공학석사학위논문

석탄화력발전소 후처리 공정 선택적촉매환원장치 내의 실험적 및 수치해석적 유동분석

Experimental and numerical investigation of the flow within a selective catalytic reduction (SCR) reactor of a coal-fired power plant

2023년 2월

서울대학교 대학원

기계공학부

한 종 호

석탄화력발전소 후처리 공정 선택적촉매환원장치 내의 실험적 및 수치해석적 유동분석

Experimental and numerical investigation of the flow within a selective catalytic reduction (SCR) reactor of a coal-fired power plant

지도교수 황 원 태

이 논문을 공학석사 학위논문으로 제출함

2022년 10월

서울대학교 대학원

기계공학부

한 종 호

한 종 호의 공학석사 학위논문을 인준함

2022년 12월

위 원 장 : 최 해 천 (인)

부위원장 : 황 원 태 (인)

위 원 : 송 성 진 (인)

Abstract

A selective catalytic reduction (SCR) reactor is commonly used to remove nitrogen oxides (NO_x) from coal-fired boilers. Uniformity of the flow passing through the catalyst layer is important for increasing denitrification (de-NO_x) efficiency. In order to examine flow uniformity, this study conducted an experimental and numerical analysis of the complex internal flow within a realistic SCR model. Magnetic resonance velocimetry (MRV) was utilized to obtain non-invasive measurements of three-dimensional three-component average velocity and validate Reynolds-averaged Navier-Stokes (RANS) numerical simulations. The computational results showed similar overall flow structure compared with the MRV results. Parameters representing flow quality such as relative standard deviation (*RSD*) and recirculation zone strength (*RZS*) were calculated by integrating the flow field. These parameters have the largest value after the inlet grid area and decrease towards the catalyst reactor, and are not significantly affected by Reynolds number upstream of the catalyst layer. The recirculation zone size was analyzed using spanwise uniformity and skewness indicators. As the recirculation zone induces biased flow, the non-reacted NO_x concentration was more prominent in the outlet zone opposite of the recirculating area in the corresponding actual on-site SCR reactor. Based on this finding, a meaningful correlation between flow maldistribution and de-NO_x reaction could be deduced.

Keyword : selective catalytic reduction (SCR), denitrification (de-NO_x), recirculation zone, magnetic resonance velocimetry (MRV), Reynolds-averaged Navier-Stokes (RANS)
Student Number : 2021-23992

Table of Contents

List of Figures

List of Tables

Nomenclature

de−NOx	Denitrification
SCR	Selective catalytic reduction
CFD	Computational fluid dynamics
AIG	Ammonia injection grid
RANS	Reynolds−averaged Navier−Stokes
RSD	Relative standard deviation
MRV	Magnetic resonance velocimetry
MRI	Magnetic resonance imaging
3D3C	three−dimensional and three−component
PIV	Particle image velocimetry
SNR	Signal to noise ratio
Var	Variance
ROI	Region of interest
$VENC$	Velocity encoding
$\vec{\sigma}_V$	Velocity uncertainty
$\Delta\psi_1(\vec{r}_{ROI})$	Phase from the first acquisition
$\Delta\psi_2(\vec{r}_{ROI})$	Phase from the second acquisition
NSA	Number of signal averages
Q	Volumetric flow rate
A	Area
σ_A	The area uncertainty
σ_Q	The flow uncertainty

X	Width depth of the rectangular inlet duct
Y	Spanwise depth of the rectangular inlet duct
D	Width of the square catalyst layer
L	Distance from the grid to the first catalyst layer
ρ	Density
$\vec{v}$	Velocity vector
P	Static pressure
μ	Summation of laminar and turbulent viscosity
$\vec{g}$	Gravity
$\vec{S}$	Momentum source term
$1/\alpha$	Viscous resistance coefficient
C_2	Inertial resistance coefficient
RZS	Recirculation zone strength
w_i	Streamwise vertical velocity component
W	Mean value of streamwise velocity
N	Total number of sample data
M_0	Inlet mass flow rate
R	Velocity magnitude
I^{w}_{sym}	Lateral uniformity parameter
I^{w}_{asym}	Lateral skewness parameter
Re	Reynolds number in the catalyst layer

$n_{\mathrm{NOx,in}}$	Inlet NOx concentration
$n_{\mathrm{NOx,out}}$	Outlet NOx concentration

Chapter 1.Introduction

1.1 Study background

Nitrogen oxides such as NO and NO_2 (collectively expressed as NO_x) can generate fine dust in the atmosphere through chemical smog reactions. NO_x is detrimental not only to the environment but also to humans [1]. In the Republic of Korea, the energy industry is the third highest emitter of NO_x, following the transportation and manufacturing sector [2]. Denitrification (de−NO_x) methods such as selective catalytic reduction (SCR) have been developed to remove NOx. In SCR, NOx is removed using chemical reactions with NH_3 in a catalyst reactor. The de−NO_x process in the SCR catalyst reactor is as follows [1,3].

$$4NH_3 + 6NO \rightarrow 5N_2 + 6H_2O \quad (1)$$

$$4NO + 4NH_3 + O_2 \rightarrow 4N_2 + 6H_2O \quad (2)$$

$$2NH_3 + 2NO + NH_4NO_3 \rightarrow 3N_2 + 5H_2O \quad (3)$$

Although several factors determine the SCR de−NO_x efficiency, uniformity of flue gas velocity and NH_3 concentration are the most important [4]. Experimental studies have demonstrated an increased de−NO_x efficiency in the catalyst layer with increasing uniformity of the velocity field [5]. Thus, having a uniform velocity entering the catalyst layer is crucial. However, the overall SCR reactor structure is complex due to spatial constraints, and consists of elbows, U−bend, and abrupt expansion. These sudden changes in shape lead to

nonuniform flow distribution [6]. Therefore, various structures are installed inside the SCR reactor to improve flow uniformity.

Since the installed structure is complex, most studies have utilized computational fluid dynamics (CFD) to analyze the flow in the SCR reactor. Gao et al. studied NH_3 slip changes by shifting the location and number of guide plates and mixer shape in the SCR de-NO_x system for a 600 MW boiler [7]. Lei et al. arranged flow-guided internal structures such as static mixers, porous plates, and guide plates to optimize the SCR flow [8]. By changing the static mixer location, Sohn et al. improved NH_3 mixing and flow velocity uniformity [9]. This study also investigated the effect of the number of ammonia injection grid (AIG) nozzles on SCR operation. Liu et al. examined the optimal flow deflector arrangement in a low volatile coal-fired 330 MW boiler [10]. A full-scale on-site experiment was conducted for SCR flow field optimization. Sun et al. conducted a CFD simulation of perforated plates with structural and positional variations for the SCR system of a diesel engine [11]. The above studies used Reynolds-averaged Navier-Stokes (RANS) models. In contrast, Shang et al. performed large eddy simulation of the transient multi-species flow in the SCR system of a 310 MW coal-fired boiler [12]. Various small recirculation zones could be observed within the instantaneous flow, which affect the mixing quality.

A few combined numerical and experimental studies have also been conducted. Xu et al. simulated the influence of a gate leaf, hybrid

grid, and straightener on the flow velocity and NH_3 concentration distribution in a 300 MW coal-fired power plant, and a 1:12 scale model experiment verified the simulation results [13]. Liu et al. decreased the nonuniformity of flue gas velocity using corner vane cascades and rectifier grills, and the reliability of the numerical results was verified through a cold test of a 1:15 scale SCR model [14]. Yang et al. examined the velocity field, ammonia concentration distribution, temperature distribution, gas incident angle, and system pressure drop by changing the guide vane and AIG [15].

However, not many experimental studies have properly analyzed the overall 3D flow structure within an SCR system. Most studies have used a single-point anemometer [14 - 17], which is an invasive flowmeter that disrupts the local flow structure. This anemometer needs to be traversed within the SCR system, and thus it is difficult to obtain a fully resolved 3D flow structure. Furthermore, simple uniformity indices such as the relative standard deviation (*RSD*) have been used to analyze the flow, but since they are scalars they cannot adequately represent the local flow distribution and can thus lead to inaccurate interpretation [18].

1.2 Purpose of research

To overcome experimental limitations of previous SCR studies, magnetic resonance velocimetry (MRV) can be utilized. MRV is a non-invasive flow measurement method using medical magnetic

resonance imaging (MRI), which can acquire the three-dimensional and three-component (3D3C) mean velocity field within complex geometries [19]. Elkins et al. used MRV to measure the mean velocity field in a gas turbine blade internal cooling passage model with a complex 180° bend structure [20]. The MRV results were similar with those from particle image velocimetry (PIV) measurements. Benson et al. utilized MRV to quantitatively visualize the complex 3D turbulent flow structure within a U-bend geometry [21]. Han et al. also examined the turbulent flow in a U-bend by comparing MRV data with a RANS model [22]. Baek et al. conducted MRV and RANS studies within a complex serpentine cooling passage inside gas turbine blade [23].

This study examines the overall 3D flow structure in a 1/70 scale SCR model of a 500 MW coal-fired power plant utilizing both MRV experiments and RANS simulations. This enables investigation of the correlation between the flow distribution and de-NO_x efficiency of an industrial-scale SCR system.

Chapter 2.Methodology

2.1 Experimental setup

The experimental setup is shown in Figure 2.1. The closed loop flow system consists of a 200 L water tank, 1.5 kW pump with inverter, valve, turbine flow meter (Omega FTB-1425), and the SCR test section. As ferrous materials are prohibited inside the MRI scan room, only the plastic test section was placed in this room, while all metal components were placed in the control room. The fluid temperature was measured using a K-type thermocouple and kept constant using a chiller, in order to keep the water viscosity constant and maintain a constant Reynolds number. A 3T Siemens MAGNETOM Trio MRI scanner (Figure 2.2) at Seoul National University Hospital was used.

The test section is shown in Figure 2.3. The SCR reactor of an actual 500 MW coal-fired power plant is modeled to 1/70 scale. A three-stage inlet flow conditioning system spreads out the jet-like flow from the inlet hose. Two sets of guide vanes, a grid, and three perforated plates appear after the flow conditioning section. The perforated plates represent the monolith catalyst layer with an Euler number of 7.37 based on on-site data. The design parameters of the perforated plate, such as porosity and thickness, are obtained from Idelchik' s handbook [24]. All parts are made of transparent acrylic to be able to observe and remove any bubbles which can alter the

flow.

Water is the working fluid, but copper sulfate was added at 0.06 M concentration to obtain a signal-to-noise ratio (SNR) suitable for MRI imaging, in reference to Benson et al. [21]. As the test section was large, three measurement areas were combined via data stitching. The time-averaged mean velocity field for each area was obtained by subtracting one "flow off" scan from the average of four "flow on" scans to eliminate background artifacts. The total scan time was approximately 5 hours. Details of experimental parameters are given in Table 2.1. Additionally, details of MRI setting parameters are represented in Table 2.2.

In MRV, the statistical velocity uncertainty in a region of interest (ROI) was given by Bruschewski et al. [25]. The measurement uncertainty is calculated using the spatial variance (*Var*) between two statistically independent images and depends on the velocity encoding (*VENC*) value which corresponds to the dynamic range of velocity, as given in Eq. (4):

$$\vec{\sigma}_V = \frac{VENC}{\pi}\sqrt{\frac{Var\{\Delta\psi_1(\vec{r}_{ROI}) - \Delta\psi_2(\vec{r}_{ROI})\}}{2 \times NSA}} \tag{4}$$

where $\vec{\sigma}_V$ is the velocity uncertainty in the ROI, $\Delta\psi_1(\vec{r}_{ROI})$ and $\Delta\psi_2(\vec{r}_{ROI})$ are the phase differences from the first and second acquisition, respectively, and NSA is the number of signal averages. The value of 2 in the denominator within the square root comes from the subtraction of two different images. The velocity uncertainty,

which was estimated from the raw data in the catalyst chamber, is 0.378, 0.376, and 0.484 cm/s in the x, y, and z directions, respectively. Higher uncertainty in the z direction is expected because of motion artifacts from the higher velocity. Nevertheless, the velocity uncertainty in the z direction is less than 8.0% of the mean velocity for 95% confidence interval within the catalyst chamber.

The flow rate is given as $Q = A \cdot V$, where Q is the volumetric flow rate, A is the area, and V is the mean streamwise velocity within the area. The area uncertainty σ_A is the difference between the maximum and minimum possible area due to voxels where fluid and solid wall coexist. The uncertainty in flow rate σ_Q is calculated using Eq. (5):

$$\sigma_Q = \sqrt{(A \cdot \sigma_V)^2 + (V \cdot \sigma_A)^2} \tag{5}$$

The flow rate from MRV is also verified using a turbine flowmeter, and the error is approximately 1.0% between MRV and flowmeter measurements. The flow rate uncertainties of MRV and flowmeter are 9.1% and 1.1%, respectively. A summary of measurement uncertainty is given in Table 2.3.

2.2 Numerical method

The computational flow domain from inlet to outlet is given in Figure 2.4, where X and Y are width and spanwise depth of the rectangular inlet duct, respectively, D is width of the square catalyst

layer, and L is distance from the grid to the first catalyst layer. The flow domain is the same as that of the experimental model. ANSYS CFX 2021R2 was used to analyze the flow, using the steady incompressible RANS equations. Similar to the experimental condition, water was used for the working fluid, and the inlet velocity boundary condition was set such that the Reynolds number at the catalyst layer was 2.0×10^4. Due to the inlet flow development section, the inlet condition before reaching guide vane 1 was essentially a fully developed flow. In addition, atmospheric pressure was prescribed as the outlet boundary condition, and heat transfer was neglected such that each wall was treated as adiabatic.

The momentum conservation equation at steady−state and incompressible conditions is given by Eq. (6):

$$\nabla \cdot (\rho \vec{v}\vec{v}) = -\nabla p + \nabla \cdot (\mu[\nabla \vec{v} + \nabla \vec{v}^T)]) + \vec{S} + \rho \vec{g} \qquad (6)$$

where ρ is density, $\vec{v}$ is the velocity vector, p is static pressure, μ is the summation of laminar and turbulent viscosity, and $\vec{g}$ is gravity. Different turbulence models were tested, and the standard $k-\varepsilon$ turbulence model which is widely used in SCR studies [8 - 10,14,15] performed fairly well, and is thus employed here. The momentum source term $\vec{S}$, accounting for the effect of external resistance in catalyst layers, is given by Eq. (7):

$$\vec{S} = -\left(\frac{\mu}{\alpha}\vec{v} + C_2 \frac{1}{2}\rho|\vec{v}|\vec{v}\right) \qquad (7)$$

where $1/\alpha$ and C_2 are viscous and inertial resistance coefficients, respectively. However, we ignore the viscous effect here because

the turbulent flow is inertia dominant at high Reynolds numbers [26]. Therefore, only the inertial resistance coefficient was considered and set to 1842 m^{-1}, referring to measurement data in industrial handbooks [24].

A grid dependency test was conducted by increasing the number of mesh points as shown in Figure 2.5, and examining the overall pressure drop and recirculation zone strength (*RZS*). *RZS* is an index that represents the relative amount of recirculating flow compared to the inlet flow, and will be explained in more detail in the following section. The grid test is halted when the residual pressure drop and *RZS* are less than 0.5%. Because the pressure drop and *RZS* converged at 19.9 M mesh points, numerical analysis was conducted using this number of grid points.

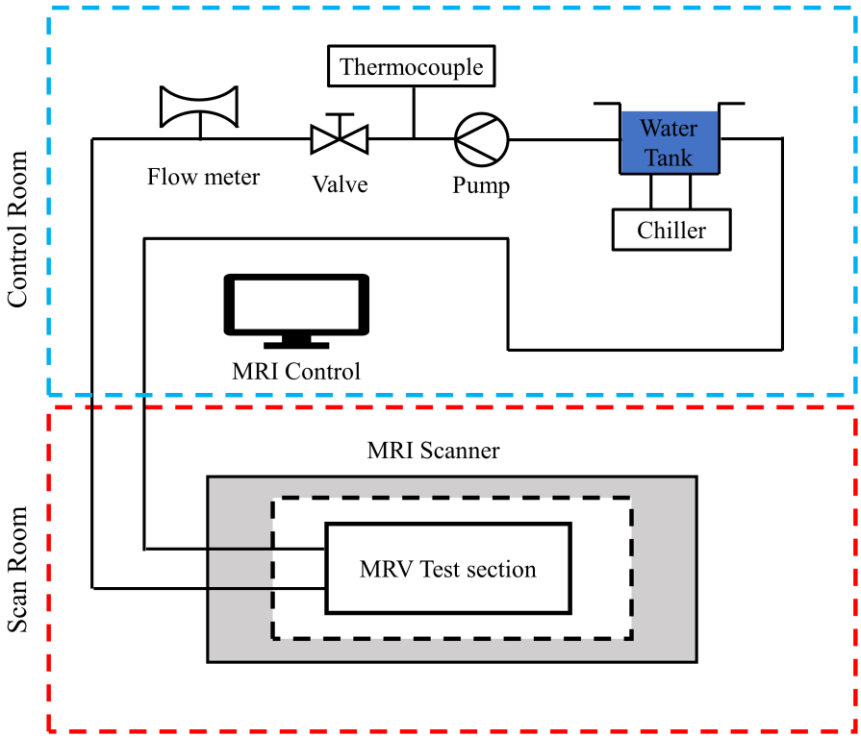

Figure 2.1 Schematic of experiment.

Figure 2.2 Experimental setup ready to be placed in the MRI scanner.

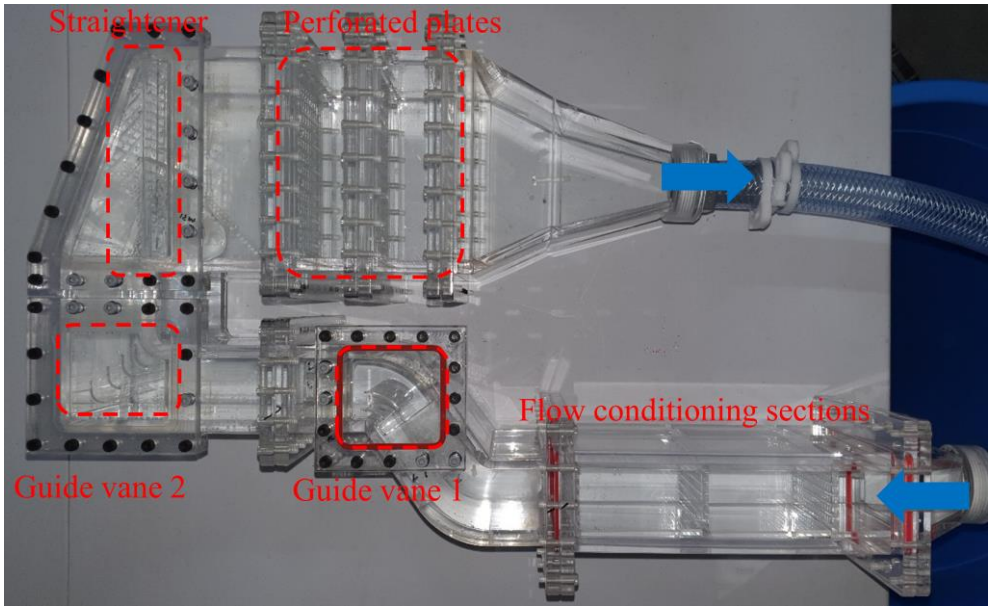

Figure 2.3 Selective catalytic reduction (SCR) reactor test section.

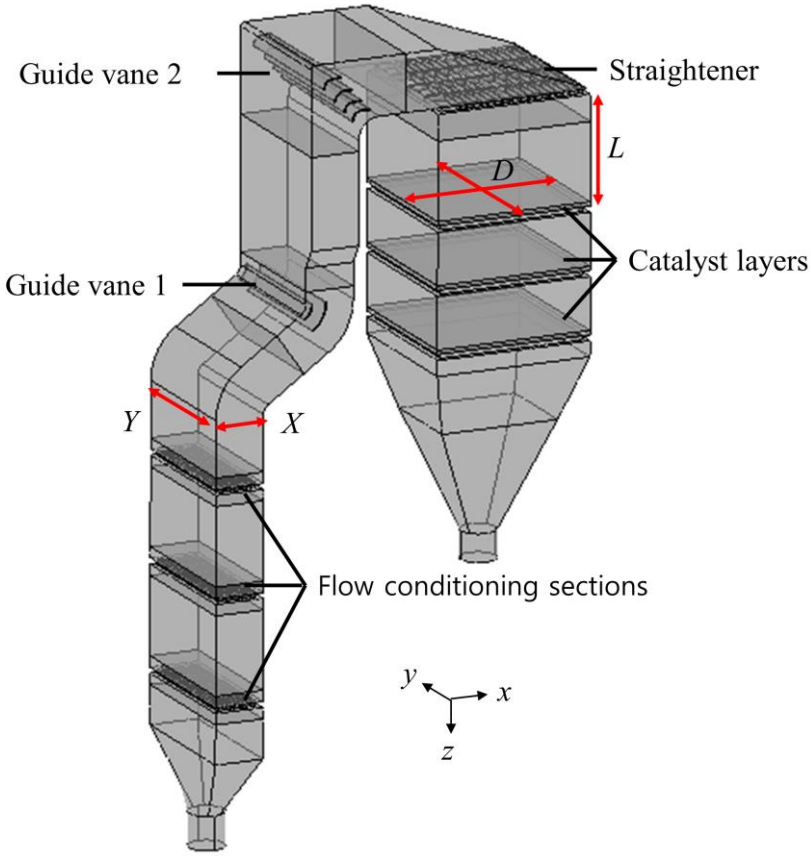

Figure 2.4 SCR structure for CFD analysis.

.

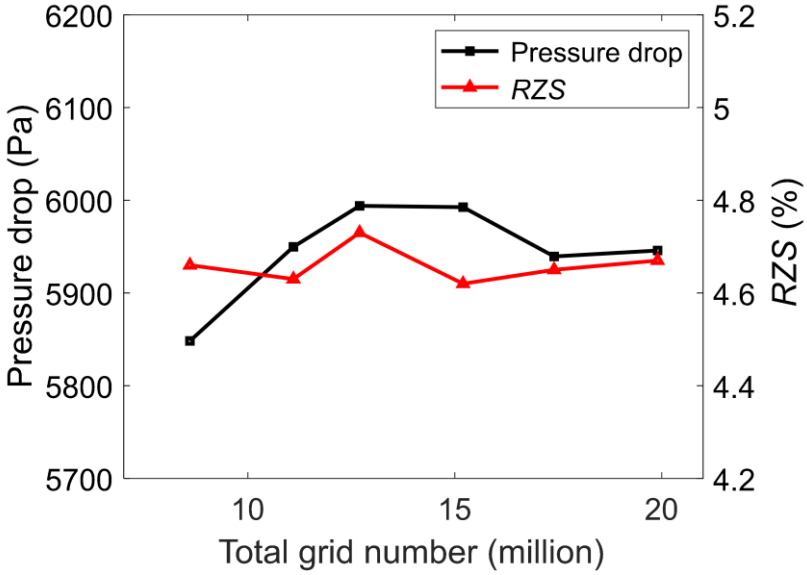

Figure 2.5 CFD grid dependency test.

Table 2.1 Experimental parameters

Flow parameters	
Fluid	0.06 M copper sulfate water solution
Volume flow rate	143 LPM
Temperature	29° C
Reynolds number	2.0×10^4 (catalyst layer)

Table 2.2 MRI settings

Scan parameters	
Flip angle	15 deg
Repetition time (TR)	27.15 ms
Echo time (TE)	4.1 ms
Bandwidth	579 Hz/px
Voxel size ($x \times y \times z$)	$2 \times 2 \times 2$ mm
VENC ($x \times y \times z$)	100 cm/s, 100 cm/s, 150 cm/s
Coil elements	Body coil, Spine coil
Field of view ($x \times y \times z$)	$384 \times 288 \times 160$ mm (3 parts stitching)
Scan time for single run	20.5 min
Number of repetitions	4 "flow on" and 1 "flow off"

Table 2.3 Uncertainty of velocity and flowrate in the ROI

Velocity		
σ_u (x−dir.)	σ_v (y−dir.)	σ_w (z−dir.)
0.378cm/s	0.376 cm/s	0.484 cm/s
Volumetric flowrate		
Flow rate (MRV)	143.5 ± 13.0 L/min	
Flow rate (Flowmeter)	142.1 ± 1.5 L/min	

Chapter 3.Results and Discussion

3.1 Flow evaluation indices

Various parameters were used to evaluate the flow. *RSD* can evaluate flow uniformity and is thus utilized as an overall indicator of SCR reactor flow quality. It is defined in Eq. (8):

$$RSD(\%) = \frac{1}{W}\sqrt{\frac{\sum_{i=1}^{N}(w_i - W)^2}{N-1}} \times 100 \qquad (8)$$

where w_i is the streamwise vertical velocity component within the SCR reactor, W is the mean value, and N is the total number of sample data. In this study, *RSD* evaluates the flow uniformity in different planes upstream of the catalyst section.

Flow separation occurs because of 90° turns within the SCR reactor [8]. Therefore, it is necessary to understand the extent of these flow separation regions. In order to estimate the ratio of recirculating flow to inlet flow, Zhu et al. used the flow parameter *RZS* given in Eq. (9) [27]:

$$RZS = \frac{1}{M_0}\int\left(\frac{\sqrt{w^2} - w}{2}\right)\rho dA \qquad (9)$$

where M_0 is the inlet mass flow rate, and w is the vertical velocity component. The term $\sqrt{w^2} - w$ effectively only samples negative streamwise velocity, as it is zero for positive velocity. In this study, we multiplied Eq. (9) with 100 to obtain the percentage of recirculating flow.

The recirculation flow causes the *RSD* to aggravate upstream of

the catalyst reactor, but since this value is a scalar it fails to represent the local flow distribution [18]. Moonen et al. (2007) decomposed the velocity component into symmetric and asymmetric functions with respect to the channel centerline, in order to evaluate the spatial flow quality [28], as shown in Eq. (10):

$$w(x) = w_{\mathrm{sym}}(x) + w_{\mathrm{asym}}(x) \tag{10}$$

where $w_{\mathrm{sym}}(x) = w_{\mathrm{sym}}(-x)$ is the symmetric streamwise velocity function, and $w_{\mathrm{asym}}(x) = -w_{\mathrm{asym}}(-x)$ is the asymmetric streamwise velocity function. The spanwise uniformity and skewness can be obtained by integrating these symmetric and asymmetric streamwise functions in the spanwise direction as defined in Eqs. (11) and (12):

$$I_{\mathrm{sym}}^{w}(x,z) = \frac{\int w_{\mathrm{sym}}^{2}(x,y,z)dy}{\int R^{2}(x,y,z)dy} \tag{11}$$

$$I_{\mathrm{asym}}^{w}(x,z) = \frac{\int w_{\mathrm{asym}}^{2}(x,y,z)dy}{\int R^{2}(x,y,z)dy} \tag{12}$$

where R is the velocity magnitude, and I_{sym}^{w} and I_{asym}^{w} are parameters describing spanwise uniformity and skewness, respectively. The streamwise velocity component in the vertical direction (w) is important in the SCR reactor, and therefore we mainly examine this component of velocity in this study.

3.2 SCR inlet flow

The inlet flow features are first analyzed, since the inlet section has an important effect on the downstream flow development. Figure 3.1 (a) and (b) show the normalized streamwise velocity profile along

the x−direction and y−direction centerlines of a plane after the last inlet grid, which is represented by the gray rectangle in Figure 3.1(c). The velocity is normalized by the inlet average velocity W. X is the width of the inlet along the x−axis, and Y is the spanwise thickness along the y−axis. The error bars represent the measurement uncertainty of the streamwise velocity in the inlet section, for 95% confidence interval. The x−direction centerline velocity profile is higher at the center and skewed to the right, as can be seen in Figure 3.1(a), because the inlet duct is bent in the right direction. The MRV and CFD results are similar, except for slight overestimation of the CFD at the right side. The centerline velocity profile along the y−direction has a more symmetrical shape, as depicted in Figure 3.1(b), with CFD matching the experimental results fairly closely. The RSD of the MRV and CFD results within the gray plane in Figure 3.1(c) are both quite similar at 40.8% and 39.5%, respectively. Thus, it has been confirmed that both MRV and CFD have a similar inlet flow field.

3.3 Flow non−uniformity

As mentioned earlier, abrupt changes in geometry lead to flow maldistribution [6]. The overall SCR model in this study is shaped like a 180° turning duct. The local flow structure is depicted in Figure 3.2. Figure 3.2(a) shows the velocity magnitude contour from CFD at the y/D = 0.45 plane, normalized by the mean inlet velocity. As the flow turns 90° in the downward direction, it passes through

a straightener. However, even with this straightener, a large recirculation zone is visible at the left side [8], along with several smaller wakes after the grid. The flow structure obtained using MRV is shown in Figure 3.2(b). The zero-velocity iso-surface is marked with a red color, while ignoring wall slip. A similar large recirculation bubble can be observed, extending almost to the first catalyst layer. Therefore, it has been confirmed that significant flow non-uniformity is present within the catalyst chamber.

The recirculation zone should be analyzed in more detail as the upstream flow uniformity in the catalyst reactor is important for SCR de-NO_x efficiency. A schematic of the straightener utilized to maintain flow uniformity when passing through the 90° elbow region is shown in Figure 3.3(a). This design is based on an actual straightener installed in a coal-fired power plant at Korea Western Power Co., Ltd. The grid consists of four symmetric rows. Locations of three representative horizontal planes (z/L = 0.1, 0.5, and 0.9 where L is the length of the reactor between the straightener and the first catalyst layer) are depicted in Figure 3.3(b). As the straightener structure has a symmetrical shape, lines (a) - (f) are drawn on one side for each plane, corresponding to the midpoint of each row (y/D = 0.125 and 0.375). The flow distribution along these lines are discussed below.

The streamwise velocity (w) distribution in cross-sections z/L = 0.1, 0.5, and 0.9 are shown in Figure 3.4. The velocity is normalized

by the average velocity in the catalyst reactor, W_{bulk}. The in-plane secondary flow is also shown via velocity vectors. In the z/L = 0.1 plane, multiple slotted jets are observed in each row due to the grids in the straightener, for both MRV and CFD results. However, a drop in streamwise velocity occurs close to the vertical wall and in the center after the middle triangular rib. This can also be seen in the normalized streamwise velocity profiles in Figure 3.5 for lines (a) and (b) from Figure 3.3. It should be noted that the error bars are similar in size to the symbols, and thus difficult to see. The CFD matches the MRV results fairly well for line (a) at y/D = 0.125, but displays more fluctuation for line (b) at y/D = 0.375. The fluctuations are also corroborated with the large RSD for this z/L = 0.1 plane, which is 98.0% for CFD, compared to 89.8% for MRV. The CFD has a higher value than that of MRV due to these fluctuations, which is likely caused by the underestimation of turbulent mixing in CFD. It should be noted that the secondary flow velocity vectors in Figure 3.4 for this plane are mostly parallel to the x-axis, due to the horizontal flow inertia just before the 90° vertical bend.

In the z/L = 0.5 plane in Figure 3.4, the flow reversal is stronger within the larger recirculation region, compared to the z/L = 0.1 plane. The expansion of the recirculation zone can also be confirmed by comparing the span of negative velocity in lines (c) and (d), as depicted in Figure 3.5. It can be seen that the CFD results match those of MRV fairly well. As the slotted jet flow from the straightener

is mixed along the streamwise direction, *RSD* decreases to 70.4% and 74.6% for CFD and MRV, respectively. The mixing induces a secondary flow with a structure similar to a Dean vortex occurring in transverse planes of curved pipe flow observed by Dean and Hurst [29]. There are two pairs of secondary flows in Figure 3.4, small and large. Similar large vortices on the right side are measured for both MRV and CFD results. In contrast, due to asymmetric flow within the recirculation zone, small asymmetrical vortices on the left side are formed in the MRV result.

Mixing continues in the streamwise direction and thus the flow is fairly uniform in the z/L = 0.9 plane just before entering the first catalyst layer, as shown in Figure 3.4. The recirculation zone has mostly ended, as negative velocity hardly exists at the left. Likewise, velocity profiles for lines (e) and (f) in Figure 3.5 show positive values near x/D = 0. The MRV and CFD results match fairly well except near x/D = 1 for the (f) line. This could possibly be due to the CFD catalyst layer modeling. The physical blockage from the catalyst layer can increase the upstream flow velocity before it passes through the perforated plate [30], but the porous media modeling does not account for this. Due to the increased flow velocity upstream of the catalyst layer in the experiment, the *RSD* is higher at 43.3% for MRV and 36.0% for CFD. Most secondary flow is directed to the left as the recirculation bubble closes and the flow replenishes this region, as shown in Figure 3.4.

Although asymmetry occurs due to the recirculation flow, the overall results of MRV and CFD show a relatively good match for each plane. The summary of the *RSD* in each plane is given in Table 3.1.

The Reynolds number was limited to 2.0×10^4 upstream of the catalyst layer, due to experimental constraints. However, real SCR operation has a Reynolds number on the order of 10^5 to 10^6. Therefore, investigating the sensitivity of the results at various Reynolds numbers is necessary. Figure 3.6 represents the variation of in-plane *RSD* and *RZS* along the streamwise direction when the Reynolds number is increased from experimental to real conditions. The uncertainties of *RSD* and *RZS* are 11.3% and 12.0% for 95% confidence interval, respectively. Both have maximum values at $z/L = 0$ immediately after the straightener due to the alternating slotted jet flow and wakes, then decreases rapidly until $z/L = 0.1$ before monotonously decreasing downstream. As the Reynolds number increases, the *RSD* does not change significantly, as shown in Figure 3.6(a), which is similar to Dutta et al. [31]. The MRV and CFD results overall match well, but modeling the catalyst layer as a perforated plate for MRV and porous media for CFD is likely the cause of the discrepancy at $z/L = 1$. In contrast, for *RZS*, the graph converges to the real condition as the Reynolds number increases. Thus, determining flow characteristics with only *RSD* is not sufficient [18]. Overall, the trends of *RZS* for MRV and CFD results are similar, but

the results at Re = 2.0 × 10^4 for CFD is lower than that of the MRV value after z/L = 0.25, because the $k-\varepsilon$ model underestimates the extent of recirculating flow [32].

3.4 Recirculation zone analysis

Flow analysis of MRV data using the spanwise uniformity and skewness parameters from Eqs. (10) - (12) are given in Figure 3.7. Figure 3.7(a) represents the streamwise velocity divided into symmetric and asymmetric components with reference to the centerline y/D = 0.5. The square symbol is the velocity magnitude R in Eqs. (11) and (12). Uncertainty levels are depicted by representative error bars. The overall integration process of MRV data is depicted in Figure 3.7(b), using an example of calculating $I_{\mathrm{sym}}^{w}(x,z)$ by integrating the square of the symmetric component in the $y-$direction. Likewise, the flow structure in the catalyst reactor can be analyzed in detail in both $x-$ and $y-$directions.

Figure 3.8 shows MRV data analysis of the (a) spanwise uniformity and (b) skewness parameters in the $xz-$plane, integrated in the $y-$direction. The recirculation zone can be analyzed with contours of these parameters. After the flow turns 90° downward and passes the straightener, a large area of high symmetry is observed in Figure 3.8(a). In contrast, near the z/L = 0 and z/L = 1 regions, secondary flow is prominent due to the grid and perforated plate, and thus asymmetry becomes noticeable. The asymmetry is strong within

the area $x/D < 0.25$ due to the recirculation zone, as illustrated in Figure 3.8(b). This is also corroborated by Figure 3.8(c), which plots the streamwise velocity profile along the shear layer of the recirculation bubble, along the $x/D = 0.2$ line at $z/L = 0.4$. The streamwise flow velocity is negative at the center and positive on both sides, but also has a significant asymmetric component, which explains the asymmetry along this spanwise direction.

Figure 3.9 represents MRV results of the (a) spanwise uniformity and (b) skewness parameters in the yz-plane, integrated in the x-direction. According to the straightener grid shape in Figure 3.3(a), the flow can be divided into four major regions, as shown in Figure 3.9(a). Thus, the contour level in the center from $y/D = 0.25$ to 0.75 is different than the sides ($y/D = 0$ to 0.25 and $y/D = 0.75$ to 1). Most fluid flows in the streamwise direction after passing the grid, but positive flow appears on both sides, and negative flow occurs in the middle of the recirculation zone, as shown above in Figure 3.8(c). According to Figure 3.9(b), the asymmetry is shifted slightly to the left in the middle region because of asymmetry in the recirculation flow. Figure 3.9(c) shows the streamwise velocity profile of the $y/D = 0.5$ line in the $z/L = 0.5$ plane. The recirculation zone exists up to approximately $x/D = 0.2$. Compared with the line (d) in Figure 3.5, where recirculation occurs up to roughly $x/D = 0.1$, it can be seen that the recirculation zone is wider in the center.

The recirculation bubble can be qualitatively observed through the

skewness contour in Figure 3.8(b). For quantitative evaluation of the bubble size, $I^{w}_{\mathrm{asym}}(x,z)$ is averaged separately along the x− and z− directions. Figure 3.10(a) shows the distribution of the spanwise average skewness parameter, along the streamwise (z) direction. The high initial skewness is due to large and small (but prevalent along the x−direction) recirculating flow structures induced by the 90° elbow and straightener, respectively, as depicted in Figure 3.8(b). The small recirculating flow structures formed by the straightener mostly disappear by z/L = 0.1, and thereafter only the main large recirculation bubble persists until z/L = 0.95. The average skewness value in this region is relatively small because the skewness parameter is spatially averaged in the x−direction. The value gradually decreases, as can be observed from Figure 3.8(b). The sudden rise at the end is likely due to flow interference effects near the perforated plate. The overall length of the bubble in the z− direction is approximately 0.90 - 0.95 L, which is similar to the RZS result in Figure 3.6(b). Figure 3.10(b) shows the streamwise average skewness parameter along the spanwise (x) direction. The average skewness is strongest at x/D = 0.16 (corresponding to the edge of the bubble shear layer) and decreases up to x/D = 0.25. The bubble width can be considered to be roughly 0.25 D, as can be observed in Figure 3.8(b).

3.5 Relationship between non−uniformity and de−

NO_x efficiency

The de−NO_x efficiency η_{de-NOx} is represented by Eq. (12):

$$\eta_{de-NOx} = \frac{n_{NOx,in} - n_{NOx,out}}{n_{NOx,in}} \quad (12)$$

where $n_{NOx,in}$ and $n_{NOx,out}$ are catalyst reactor inlet and outlet NO_x concentrations, respectively. In other words, $n_{NOx,out}$ corresponds to the unreacted NO_x concentration. Large de−NO_x efficiency indicates small NO_x concentration at the outlet. Because de−NO_x efficiency decreases due to flow non−uniformity within the SCR reactor [5], non−reacted NO_x can be inferred via CFD from a fluid mechanic point of view. The non−reacted NO_x data obtained by 40 measurement points (4 rows x 10 columns) in the outlet of an actual SCR reactor of a 500−MW coal−fired power plant in operation at Korea Western Power is shown in Table 3.2.

CFD simulations of this actual SCR reactor at real conditions of Reynolds number 10^6 were conducted to assess the correlation between the non−reacted NO_x and flow structure, as shown in Figure 3.11. The recirculation zone is evident at the inner side of the catalyst chamber, upstream of the 1st catalyst layer. The outlet is divided into rows (a) - (d) with the same cross−sectional area as in Table 3.2, for comparison with the on−site measurement data. Figure 3.12 shows *RSD* results of the measured NO_x concentration and calculated streamwise velocity. The velocity index of Eq. (8) which originally uses streamwise velocity is substituted with the NO_x concentration value. The *RSD* is the largest in section (d), followed by section (a),

for both NO_x concentration and streamwise velocity. It is interesting to note that the trends between these two values are quite similar. Therefore, we can infer that the flow bias due to recirculation induces uneven NO_x chemical reactions.

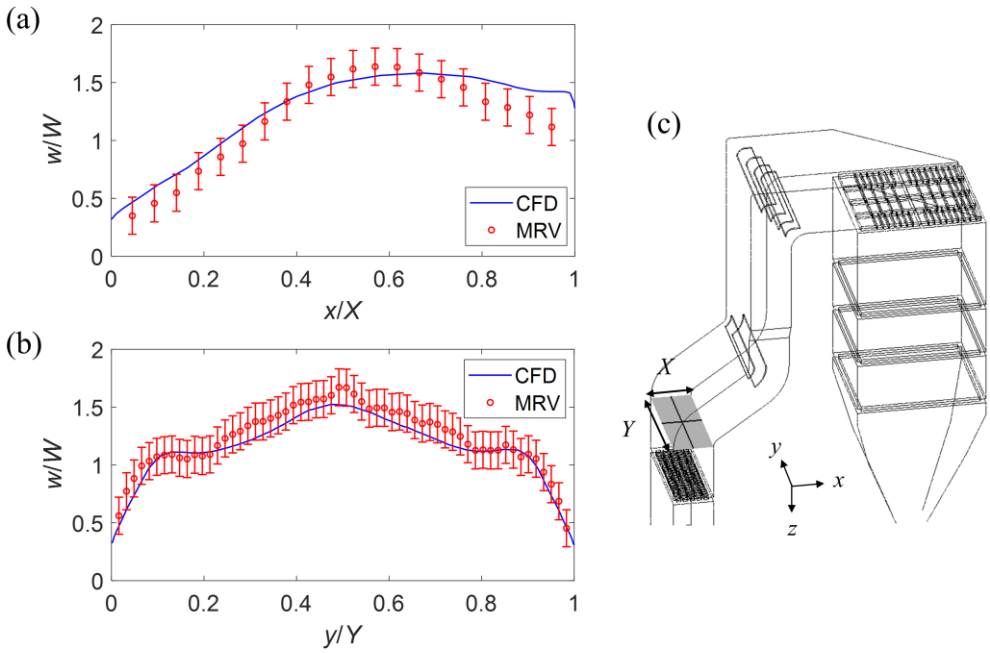

Figure 3.1 Inlet (a) x−direction and (b) y−direction centerline velocity profile, (c) schematic of SCR structure.

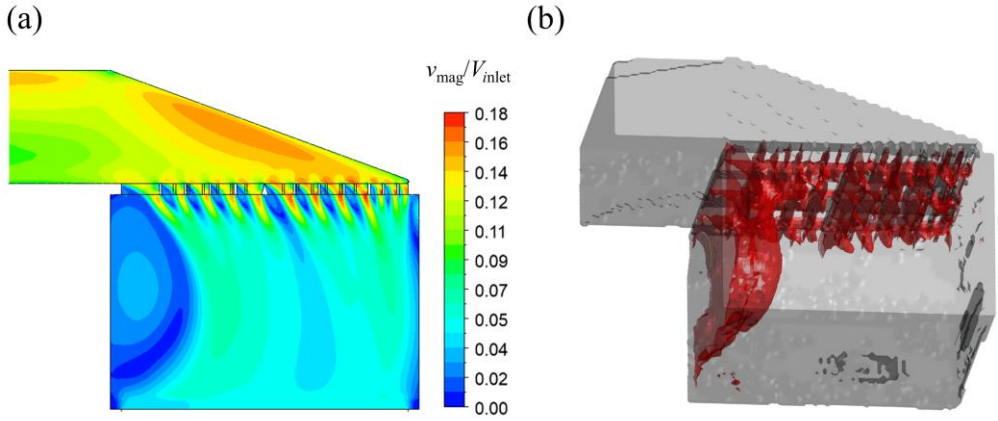

Figure 3.2 (a) CFD velocity magnitude contour in the y/D = 0.45 plane, (b) MRV zero−velocity iso−surface.

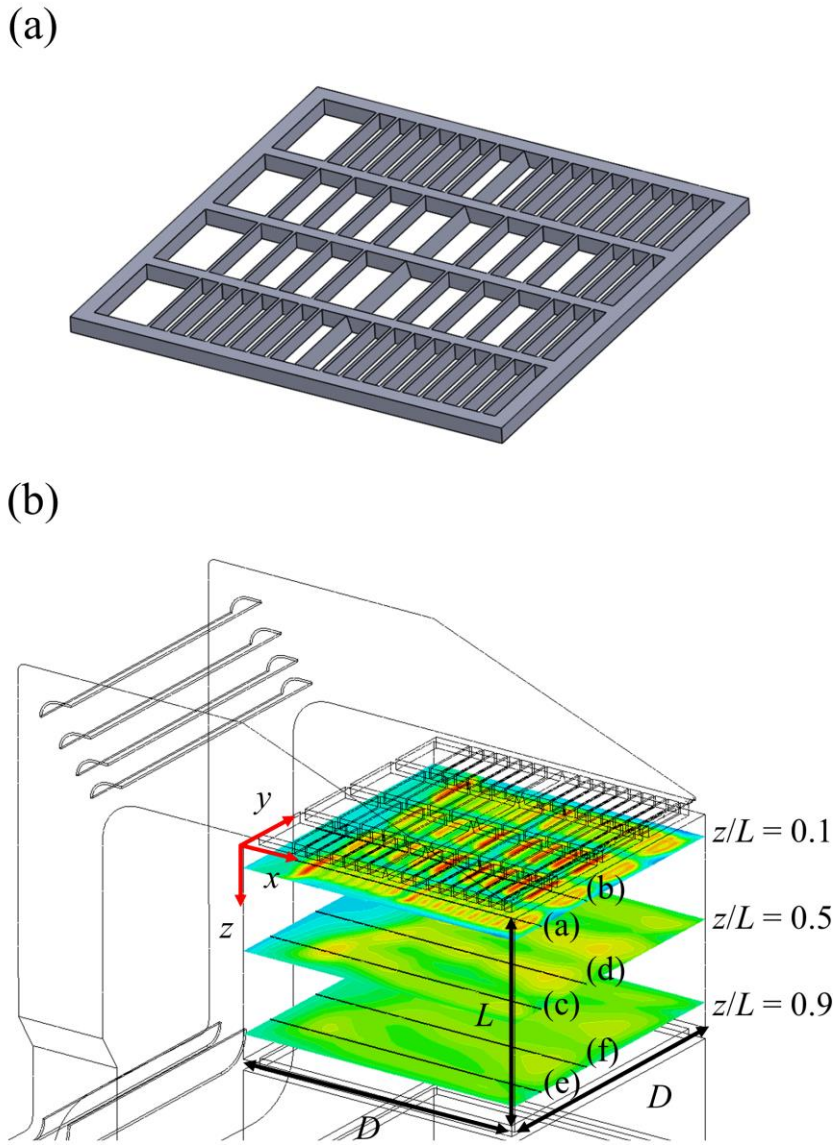

Figure 3.3 Schematic of (a) straightener and (b) SCR cross sections upstream of the catalyst layer.

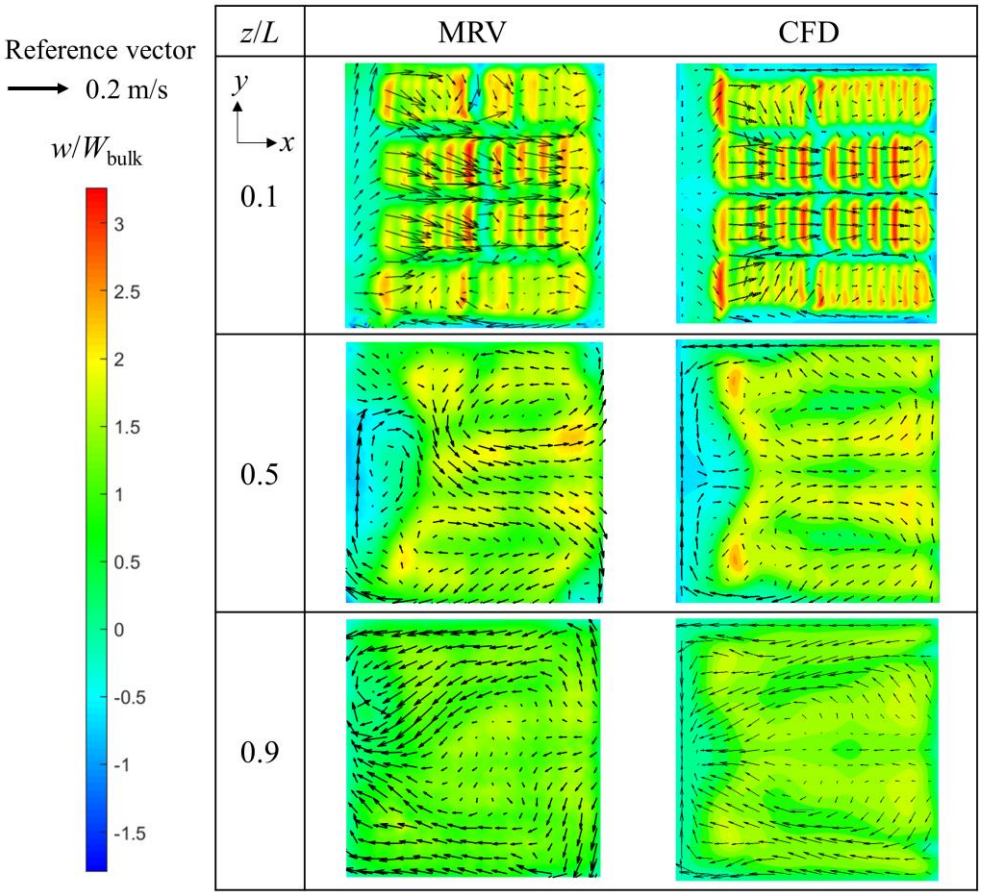

Figure 3.4 Normalized streamwise velocity distribution and secondary flow pattern in each cross−section (z/L = 0.1, 0.5, 0.9).

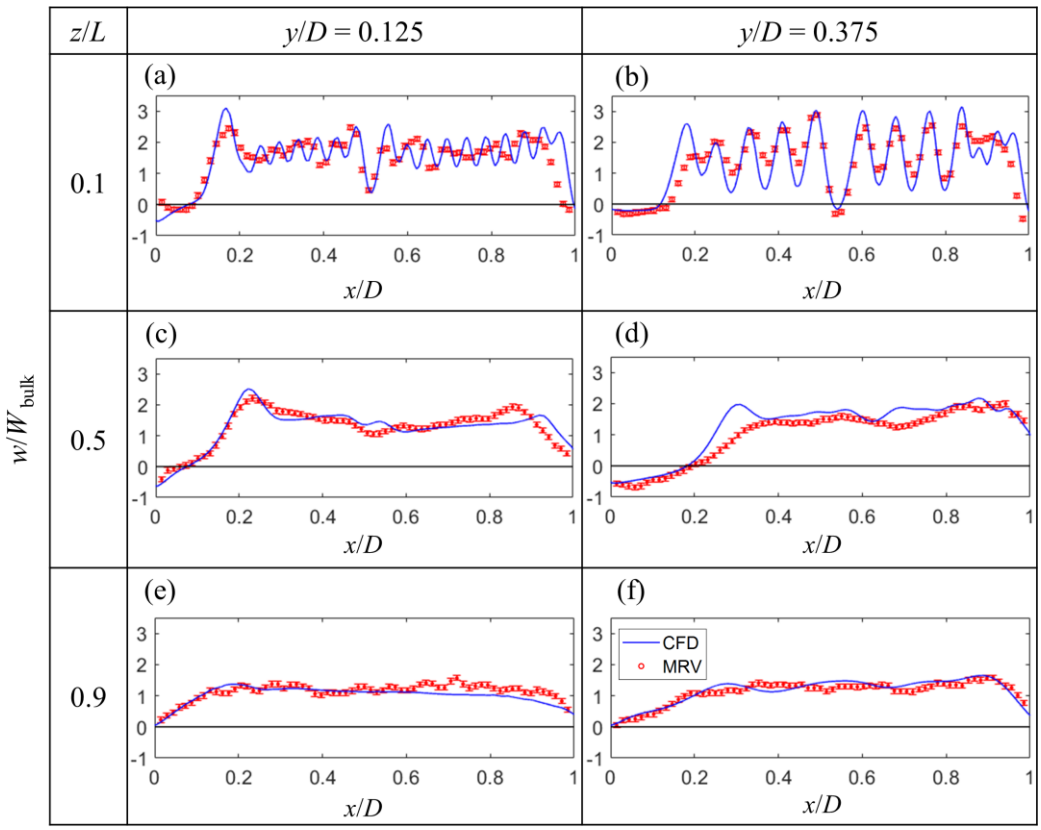

Figure 3.5 Normalized mean streamwise velocity profile at lines (a) – (f) in each cross-section (z/L = 0.1, 0.5, 0.9).

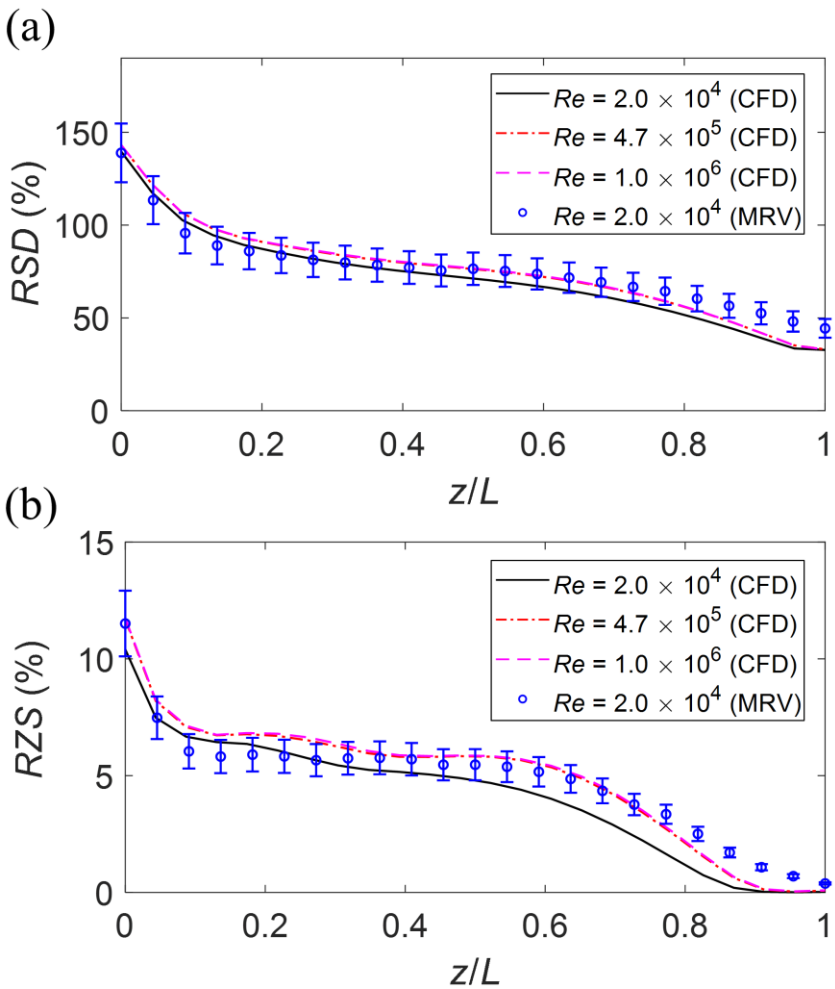

Figure 3.6 Reynolds number sensitivity for (a) *RSD* and (b) *RZS*.

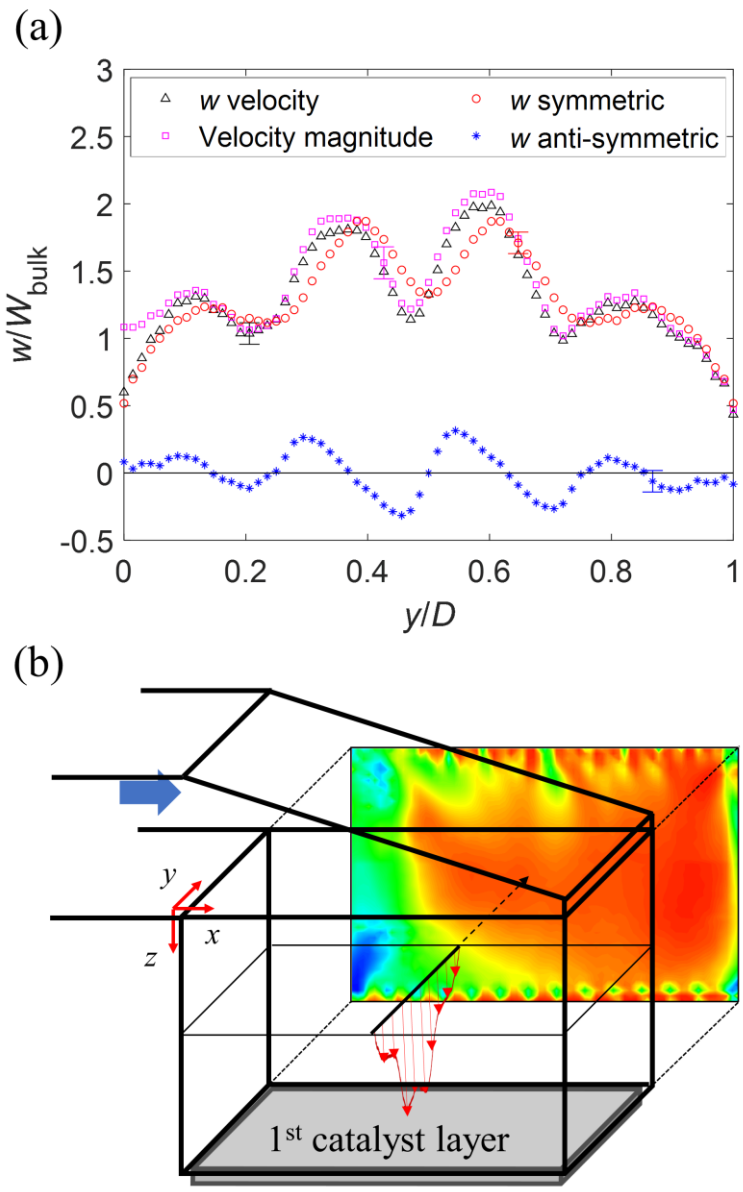

Figure 3.7 MRV data component of (a) streamwise velocity along the $x/D = 0.5$ line in the $z/L = 0.5$ plane, separated into symmetric (about $y/D = 0.5$) and anti−symmetric velocity. (b) Square of symmetric velocity component integrated along a horizontal line in the spanwise direction within the test section, for MRV data.

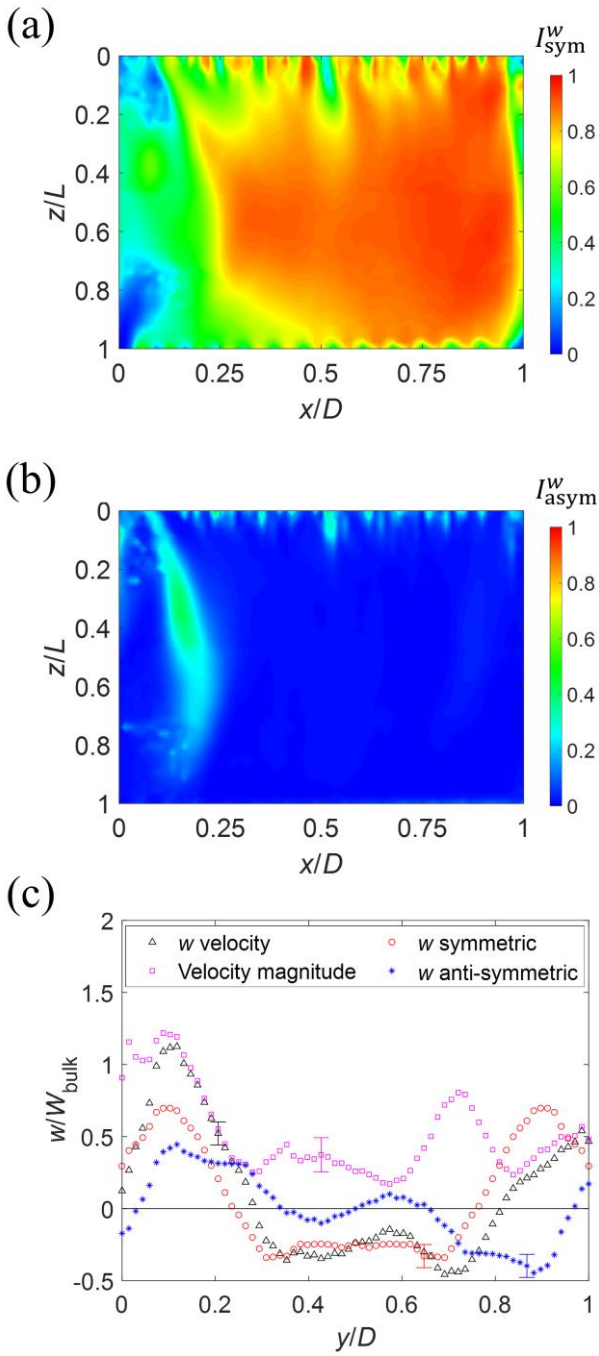

Figure 3.8 MRV data component of (a) symmetric velocity squared and (b) asymmetric velocity squared integrated along a horizontal line in the spanwise y−direction of the test section. (c) Separation of streamwise velocity components for the x/D = 0.2 line within the z/L = 0.4 plane.

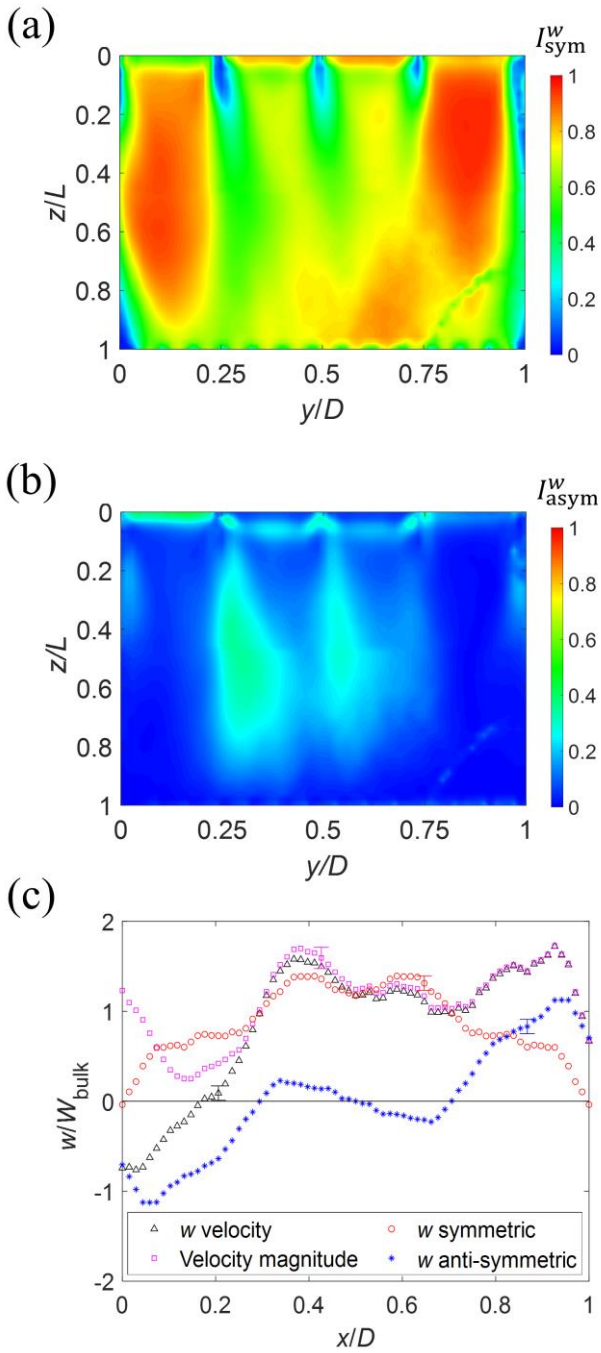

Figure 3.9 MRV data component of (a) symmetric velocity squared and (b) asymmetric velocity squared integrated along a horizontal line in the x−direction of the test section. (c) Separation of streamwise velocity components for the y/D = 0.5 line within the z/L = 0.5 plane.

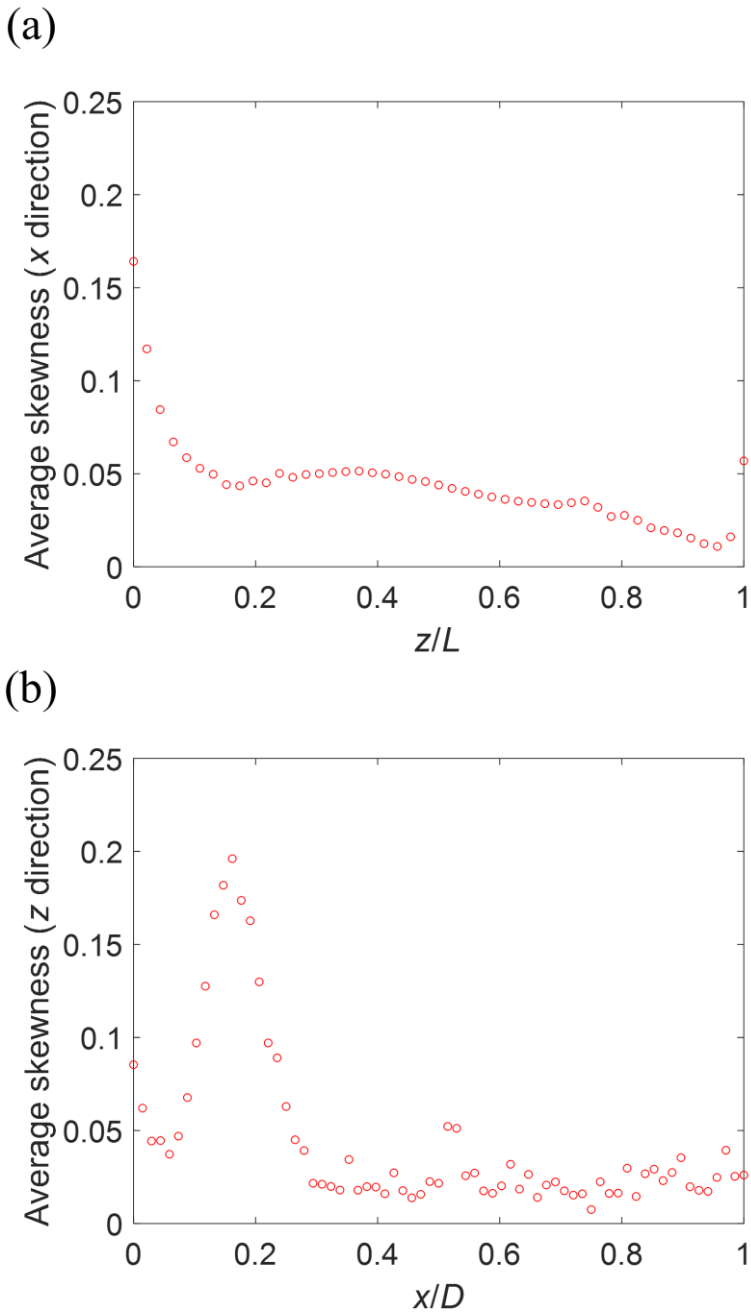

Figure 3.10 (a) Spanwise (x−direction) average skewness along the streamwise direction and (b) streamwise (z−direction) average skewness along the spanwise direction, for MRV data.

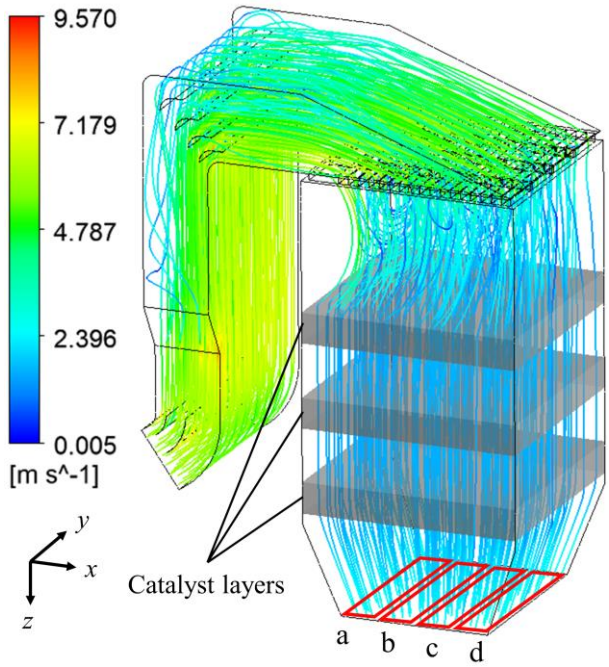

Figure 3.11 Streamline velocity of real-scale SCR reactor from CFD.

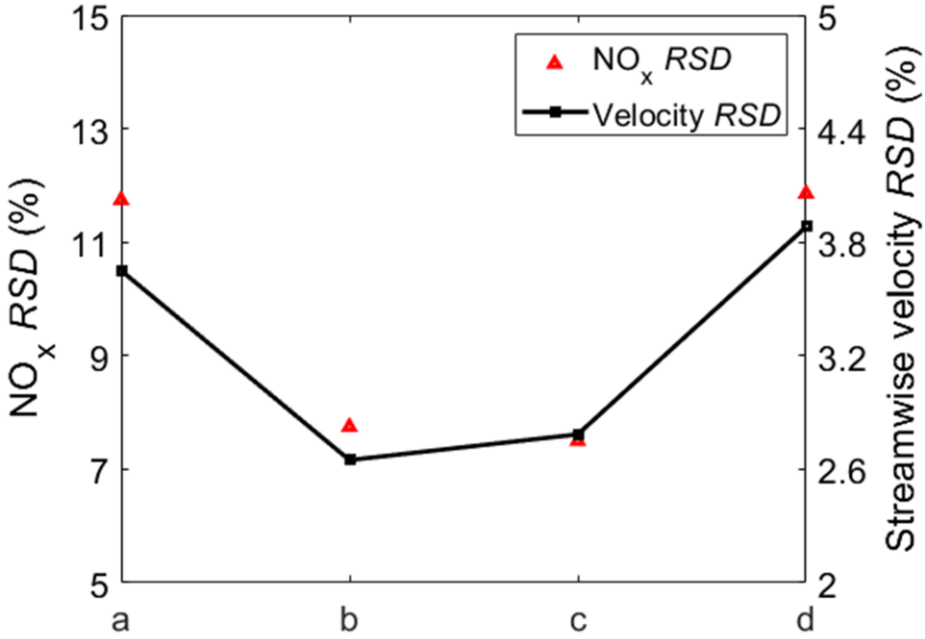

Figure 3.12 *RSD* comparison of NO_x concentration and streamwise velocity.

Table 3.1 *RSD* of MRV and CFD in each plane

z/L	MRV	CFD
0.1	89.6%	98.0%
0.5	74.6%	70.4%
0.9	43.3%	36.0%

Table 3.2 On-site SCR outlet NO_x data [ppm]

	a	b	c	d
1	33	36	41	41
2	32	33	32	30
3	34	36	34	35
4	39	37	36	30
5	38	34	37	41
6	30	31	35	36
7	31	37	40	34
8	38	38	37	42
9	40	37	39	38
10	42	41	38	38
Mean	35.7	36.0	36.9	36.5

Chapter 4.Conclusion

The internal flow within an SCR reactor of a coal-fired power plant has been examined using experimental and numerical methods, where RANS simulations were validated using magnetic resonance velocimetry (MRV) results. The flow structure in the SCR reactor was analyzed by calculating relative standard deviation (*RSD*), recirculation zone strength (*RZS*), and spanwise uniformity and skewness parameters. Representative results are as follows.

Due to flow separation induced by an abrupt change in flow path, a large recirculation zone is created within the main reactor, upstream of the catalyst layer. In terms of flow non-uniformity, after passing the straightener grid installed in the 90° bend, the *RSD* decreased as secondary flow was generated. The CFD result has a higher *RSD* right after the grid compared with experimental results, likely due to underestimation of turbulent mixing. However, the *RSD* rapidly decreased along the streamwise direction. On the other hand, the *RZS* was underestimated due to limitations of the $k-\varepsilon$ turbulence model. When the Reynolds number was increased to real conditions, no significant changes in *RSD* and *RZS* were observed.

Detailed analysis was conducted on the recirculation zone. The spatial velocity distribution was assessed via spanwise uniformity and skewness parameters. An asymmetric 3D flow structure due to the complex recirculating flow was revealed. In addition, the flow was more concentrated in the center region. The recirculation zone

almost reaches the catalyst layer and is 25% of the reactor width in the spanwise direction. The *RSD* of fluid velocity and NO_x concentration at the reactor outlet had similar trends, and it was inferred that the nonuniform flow caused by recirculation deteriorates the de−NO_x process.

In the future, an additional catalyst layer will be added upstream of the initial layer and the effect on the flow structure will be investigated. In addition, optimization of SCR reactor geometry features will be conducted to improve flow uniformity and de−NO_x efficiency.

Acknowledgement

This work was supported by Korea Western Power CO., Ltd. (No. 2020-OPER-0 and 2021-consignment-05) and the Institute of Advanced Machines and Design at Seoul National University.

Bibliography

1. Forzatti, P., I. Nova, and E. Tronconi, *Enhanced NH_3 selective catalytic reduction for NOx abatement*, Angewandte Chemie, 2009, **121**: p. 8516-8518.
2. KOSIS, NOx. https://kosis.kr/search/search.do, (accessed 07 July 2022).
3. Lietti, L., I. Nova, E. Tronconi, and P. Forzatti, *Transient kinetic study of the SCR-DeNOx reaction*, Catalysis Today, 1998, **45**: p. 85-92.
4. Lang, E., P. Drtina, F. Streiff, and M. Fleischli, *Numerical simulation of the fluid flow and the mixing process in a static mixer*, International Journal of Heat and Mass Transfer, 1995, **38**(12): p. 2239-2250.
5. Martin, A.P., N.S. Will, A. Bordet, P. Cornet, C. Gondoin, and X. Mouton, *Effect of flow distribution on emissions performance of catalytic converters*, SAE transactions Jornal of Fuels and Lubricants, 1998, **107**: p. 384-390.
6. Bluestein, A.M., R. Venters, D. Bohl, B.T. Helenbrook, and G. Ahmadi, *Turbulent flow through a ducted elbow and plugged tee geometry: An experimental and numerical study*. Journal of Fluids Engineering, 2019, **141**(8): p. 081101.
7. Gao, Y., Q. Liu, and L. Bian, *Numerical simulation and optimization of flow field in the SCR denitrification system on a 600 MW capacity units*, Energy Procedia, 2012, **14**: p. 370-375.
8. Lei, Z., C. Wen, and B. Chen, *Optimization of internals for selective catalytic reduction (SCR) for NO removal*, Environmental Science

and Technolgy, 2011, **45**(8): p. 3437-3444.

9. Sohn, J., I.S. Hwang, and J. Hwang, *Improvement of ammonia mixing in an industrial scale selective catalytic reduction De-NOx system of a coal-fired power plant: A numerical analysis*, Process Safety and Environmental Protection, 2021, **147**: p. 334-345.

10. Liu, X., H. Tan, Y. Wang, F. Yang, H. Mikulčić, M. Vujanović, and N. Duić, *Low NOx combustion and SCR flow field optimization in a low volatile coal fired boiler*, Journal of Environmental Management, 2018, **220**: p. 30-35.

11. Sun, K., H. Zhao, K. Zhao, D. Li, and S. Bai, *Optimization of SCR inflow uniformity based on CFD simulation*, Open Physics. 2020, **18**(1): p. 1168-1177.

12. Shang, D., B. Li, and Z. Liu, *Large eddy simulation of transient turbulent flow and mixing process in an SCR denitration system*, Chemical Engineering Research Design. 2019, **141**: p. 279-289.

13. Xu, Y., Y. Zhang, J. Wang, and J. Yuan, *Application of CFD in the optimal design of a SCR-DeNOx system for a 300 MW coal-fired power plant*, Computers and Chemical Engineering, 2013, **49**: p. 50-60.

14. Liu, H., T. Guo, Y. Yang, and G. Lu, *Optimization and numerical simulation of the flow characteristics in SCR system*, Energy Procedia, 2012, **17**: p. 801-812.

15. Yang, Y., J. Li, and H. He, *Research and proposal on selective catalytic reduction reactor optimization for industrial boiler*, Journal of the Air and Waste Management Association, 2018, **68**(7): p. 737-754.

16. Li, W.Y., S.Y. Wang, and X.M. Wang, *Model Experimental Study of*

SCR Reactor Flow Optimization in 1000MW Coal-Fired Boiler, Advanced Materials Research, 2014, **955**: p. 2177-2181.

17. Liu, X., Y. Sun, F. Xue, J. Su, and F. Chen, *Study on Flow Field Optimization for SCR System of Coal-fired Power Plants,* In: Journal of Physics: Conference Series. IOP Publishing, 2019, **1300**(1): p. 012027.

18. Barlow, J.B., W.H. Rae, and A. Pope. *Low-speed wind tunnel testing*, third ed., John Wiley & Sons, New York, 1999.

19. Elkins, C.J. and M.T. Alley, *Magnetic resonance velocimetry: applications of magnetic resonance imaging in the measurement of fluid motion*, Experiment in Fluids, 2007, **43**(6): p. 823-858.

20. Elkins, C.J., M. Markl, A. Iyengar, R. Wicker, and J.K. Eaton, *Full-field velocity and temperature measurements using magnetic resonance imaging in turbulent complex internal flows*, International Journal of Heat Fluid Flow , 2004, **25**(5): p. 702-710.

21. Benson, M.J., A.J. Banko, C.J. Elkins, D.G. An, S. Song, M. Bruschewski, S. Grundmann, D.D. Borup and J.K. Eaton, *The 2019 MRV challenge: turbulent flow through a U-bend*, 2020, **61**(6): p. 1-17.

22. Han, Y., L. Zhou, L. Bai, W. Shi, and R. Agarwal, *Comparison and validation of various turbulence models for U-bend flow with a magnetic resonance velocimetry experimen*t, Physics of Fluids, 2021, **33**(12): p. 125117.

23. Baek, S., J. Ryu, M. Bang, and W. Hwang, *Flow non-uniformity and secondary flow characteristics within a serpentine cooling channel of a realistic gas turbine blade*, Journal of Turbomachinery, 2022, **144**(9): p. 091002.

24. Idelchik, I.E., *Handbook of hydraulic resistance*, fourth ed., Hemisphere Publishing Corporation, Washington, 1986.

25. Bruschewski, M., D. Freudenhammer, W.B. Buchenberg, H.P. Schiffer, and S. Grundmann, *Estimation of the measurement uncertainty in magnetic resonance velocimetry based on statistical models*, Experiments in Fluids, 2016, **57**(5): p. 1-13.

26. Zeng, Z., and R. Grigg, *A criterion for non-Darcy flow in porous media*, Transport in Porous Media, 2006, **63**(1): p. 57-69.

27. Zhu, X., R. Li, D. Li, P. Zhang, and R. Qian, *Experimental study and RANS calculation on velocity and temperature of a kerosene-fueled swirl laboratory combustor with and without centerbody air injection*, International Journal of Heat and Mass Transfer, 2015, **89**: p. 964-976.

28. Moonen, P., B. Blocken, and J. Carmeliet, *Indicators for the evaluation of wind tunnel test section flow quality and application to a numerical closed-circuit wind tunnel*, Journal of Wind Engineering and Industrial Aerodynamics, 2007, **95**: p. 1289-1314.

29. Dean, W.R., and J.M. Hurst, *Note on the motion of fluid in a curved pipe*, Mathematika, 1959, **6**(1): p. 77-85.

30. Kim, H.B., and S.J. Lee, *Hole diameter effect on flow characteristics of wake behind porous fences having the same porosity*, Fluid Dynamics Research, 2001, **28**(6): p. 449-464.

31. Dutta, P., S.K. Saha, N. Nandi, and N. Pal, *Numerical study on flow separation in 90° pipe bend under high Reynolds number by $k-\varepsilon$ modelling*, Engineering Science and Technologhy. and International Journal, 2016, **19**(2): p. 904-910.

32 Vasilopoulos, K., I.E. Sarris, and P. Tsoutsanis, *Assessment of air*

flow distribution and hazardous release dispersion around a single obstacle using Reynolds-averaged Navier-Stokes equations. Heliyonm, 2019, **5**(4), e01482.

초 록

선택적 촉매 환원 반응 장치는 석탄 화력 발전소에서 질소산화물을 제거하기 위해 일반적으로 사용된다. 이때 촉매층을 통과하는 유동의 균일성은 탈질화 효율을 높이는 데 중요하다. 본 연구에서는 유동의 균일성을 분석하기 위해 현실적인 선택적 촉매 환원 장치 모형 내에서 복잡한 내부 유동에 대한 실험적이고 수치적인 분석을 수행했다. 자기 공명 유속계는 비침습적으로 3차원 3성분 평균 속도를 얻고 레이놀즈 평균 나비에-스토크스 수치 시뮬레이션을 검증하는데 사용되었다. 수치해석 결과는 자기 공명 유속계와 비교했을 때 유사한 유동 구조를 나타냈다. 상대 표준 편차와 재순환 영역 강도 등의 유동 분석 파라미터들을 통해 속도 성분을 적분하여 유동 분석을 했다. 이 파라미터들은 스크린판 직후 가장 큰 값을 띄다가 촉매 반응기 쪽으로 갈수록 감소하며, 촉매 반응기 상류의 유동은 레이놀즈 수에 크게 영향을 받지 않는다. 재순환 영역의 크기는 측면 방향 유동 균일성 및 불균일성 지표를 통해 분석할 수 있었다. 또한, 현장에서 계측한 미반응 질소산화물 농도 데이터와 실제 크기에서의 전산수치해석 결과를 비교를 했다. 그 결과, 재순환 영역이 편향된 흐름을 유도함에 따라, 해당 선택적 촉매 환원 반응 장치에서 발생하는 재순환 영역의 반대쪽 출구 영역에서 미반응 질소산화물 농도가 더 크게 나타났다. 이 발견을 바탕으로 유동 불균일 성이 탈질 반응 사이에서 유의미한 상관관계를 추론할 수 있었다.

주요어 : 선택적 촉매 환원, 탈질화, 유동 균일성, 재순환 영역, 자기 공명 유속계, 레이놀즈 평균 나비에-스토크스
학 번 : 2021-23992